




# The role of particle precipitation on plasma structuring at different altitudes by in-situ measurements

Lisa M. Buschmann<sup>1,\*</sup> , John W. Bonnell<sup>2</sup>, Scott Bounds<sup>3</sup>, Lasse B.N. Clausen<sup>1</sup>, Craig Kletzing<sup>3</sup> , Sigvald Marholm<sup>1,4</sup>, Wojciech J. Miloch<sup>1</sup> , Roger Roglans<sup>2</sup>, and Andres Spicher<sup>5</sup> 

<sup>1</sup> Department of Physics, University of Oslo, Problemveien 7, 0315 Oslo, Norway

<sup>2</sup> Space Sciences Laboratory, University of California Berkeley, 7 Gauss Way, Berkeley, CA 94720, USA

<sup>3</sup> University of Iowa, Iowa City, IA 52242, USA

<sup>4</sup> Department of Computational Materials Processing, Institute for Energy Technology, Instituttveien 18, 2007 Kjeller, Norway

<sup>5</sup> Department of Physics and Technology, The Arctic University of Norway, Klokkegårdsbakken 35, 9019 Tromsø, Norway

Received 21 September 2022 / Accepted 21 April 2023

**Abstract**—The plasma in the cusp ionosphere is subject to particle precipitation, which is important for the development of large-scale irregularities in the plasma density. These irregularities can be broken down into smaller scales which have been linked to strong scintillations in the Global Navigation Satellite System (GNSS) signals. We present power spectra for the plasma density irregularities in the cusp ionosphere for regions with and without auroral particle precipitation based on in-situ measurements from the Twin Rockets to Investigate Cusp Electrodynamics-2 (TRICE-2) mission, consisting of two sounding rockets flying simultaneously at different altitudes. The electron density measurements taken from the multi-needle Langmuir probe system (m-NLP) were analyzed for the whole flight duration for both rockets. Due to their high sampling rates, the probes allow for a study of plasma irregularities down to kinetic scales. A steepening of the slope in the power spectra may indicate two regimes, a frequency interval with a shallow slope, where fluid-like processes are dominating, and an interval with a steeper slope which can be addressed with kinetic theory. The steepening occurs at frequencies between 20 Hz and 100 Hz with a median similar to the oxygen gyrofrequency. Additionally, the occurrence of double slopes increases where precipitation starts and throughout the rest of the flight. In addition, strong electron density fluctuations were found in regions poleward of the cusp, thus in regions immediately after precipitation. Furthermore, by investigating the integrated power of the fluctuations within different frequency ranges, we show that at low frequencies (10–100 Hz), the power is pronounced more evenly while the rocket encounters particle precipitation, while at high frequencies (100–1000 Hz) fluctuations essentially coincide with the passing through a flow channel.

**Keywords:** Energetic particle precipitation / Ionosphere / Ionospheric irregularities / Plasma density / Power spectral density

## 1 Introduction

The high-latitude ionosphere is subject to plasma structures over a wide range of scales from 100 km down to meter-sized structures (Basu et al., 1990; Tsunoda, 1988). Smaller scale irregularities can modulate trans-ionospheric radio waves, leading to rapid fluctuations in the received phase and amplitude which are often referred to as scintillations (Carlson, 2012). Thereby, plasma structuring can disturb satellite communication systems, which may cause navigation errors or a failure of signal acquisition (Kintner et al., 2007; Yeh and Liu, 1982). Global

navigation satellite systems (GNSS) play an important role in operating aviation and marine traffic and are becoming more and more important due to higher human activity in the polar regions. Thus, more effort has been put into understanding the formation of plasma irregularities on small scales in the ionosphere in recent years (e.g. Jin et al., 2014; Kintner et al., 2007; Moen et al., 2013; Oksavik et al., 2012).

A number of different sources have been suggested for the formation of irregularities, for example, the gradient drift instability (GDI) and the Kelvin-Helmholtz instability (KHI) (Kintner & Seyler, 1985; Tsunoda, 1988; Basu et al., 1990; Keskinen & Ossakow, 1983). The GDI has its origin in the different drifts of ions and electrons in steep density gradients and is

\*Corresponding author: [lisa.buschmann@fys.uio.no](mailto:lisa.buschmann@fys.uio.no)

the dominant instability occurring in polar cap patches, regions of 100 km scale with at least twice the density as the background plasma (Crowley et al., 1996; Tsunoda, 1988). The KHI is rather driven by velocity shears in the plasma and, on the dayside, a two-step process has been proposed, where the KHI is first structuring the plasma patch entering the polar cap on which the GDI can then effectively act and further structure the patch (Carlson et al., 2007; Moen et al., 2013).

The plasma in the cusp ionosphere is subject to auroral particle precipitation, which is thought to be an important source of large-scale irregularities with long lifetimes (Kelley et al., 1982b; Moen et al., 2002, 2013). These irregularities are able to convect over large areas and can thus be further structured by the GDI and KHI (Moen et al., 2012). Recently Jin et al. (2015) found that strong scintillations can be related to particle precipitation and the cusp aurora.

Power spectra are a common tool to analyze instabilities and turbulence in a plasma, describing the cascading of the energy in the system (Frisch & Kolmogorov, 1995). It has been suggested that ionospheric plasma instabilities should be described by power laws (Kintner & Seyler, 1985; Tsunoda, 1988) and different mechanisms are thought to result in different slopes in the spectra. Past observations suggested a slope of  $p \approx -5/3$  for the initial spectral index before the steepening occurs (Kintner & Seyler, 1985). In situ measurements of the ionosphere made it possible to show that power spectra of plasma fluctuations exhibit a steeper slope for higher frequencies when plotted logarithmically. This slope steepening has been first documented for the low-latitude ionosphere with sounding rockets and satellites (Kelley et al., 1982b) and is well observed in this region (e.g. LaBelle et al. 1986; Hysell et al. 1994; Jahn & LaBelle, 1998). High-resolution measurements made it possible to show this steepening for the high-latitude F-region (Villain et al., 1986; Basu et al., 1990; Spicher et al., 2014; Ivarsen et al., 2019; Di Mare et al., 2021). The spectral index in the high-latitude ionosphere has been shown to be close to  $p_1 \approx -5/3$  at low frequencies and around  $p_2 \approx -3$  to  $p_2 \approx -5$  for high frequencies in these works. The frequencies of the spectral break have been studied for decades along with the steepening of the spectrum, but observed at a variety of different frequencies. It is still mostly unknown as to what frequency the break occurs (Tsunoda, 1988), thus, this is still of importance.

A conducting E region was found to speed up the diffusion of plasma structures in the F region (Kelley et al., 1982a, 1982b; Basu & Coppi, 1988). Additionally, electric coupling between the two regions along the magnetic field lines leads to a way for electrons to transfer between them. It was found that this coupling with a highly conductive E-region leads to a faster decay of plasma structures in the F-region compared to a less conducting E-region (Kelley et al., 1982b; Ivarsen et al., 2019). In this paper, we present results from the TRICE-2 flights, consisting of two sounding rockets flying simultaneously at different altitudes. We compare intervals with and without particle precipitation for both altitudes and investigate the differences in power spectra between these regions. While power spectra with double slopes in regions of strong fluctuations have been investigated before, the TRICE-2 campaign allows for the first time a simultaneous study at two different altitudes. We were able to confirm the spectral indices for power spectra in the ionosphere mentioned above. Additionally, we show that a double slope starts appearing when the rocket enters

the cusp, but the spectral break frequency rather follows a variation in the electric field. Furthermore, through analysis of the integrated power within the power spectra analysis, we can show that lower frequencies, thus larger scales, are more elevated during precipitation, while higher frequencies, or smaller scales, are elevated during a rise in an electric field.

The paper is divided as follows: Section 2 presents the TRICE-2 sounding rockets and the instruments on board used in this work, with an emphasis on the multi-needle Langmuir probe. Section 3 gives a brief overview of the flight conditions and the results which focus on spectral analysis of the electron density data placed in the context of observations from other instruments. Finally, the results are discussed in Section 4 and a conclusion is given in Section 5.

## 2 Instrumentation

### 2.1 TRICE-2 Sounding Rockets

The Twin Rockets to Investigate Cusp Electrodynamics (TRICE-2) mission is a NASA mission that is part of the Grand Challenge Initiative – Cusp (GCI – Cusp) (Moen et al., 2018). The mission consists of two rockets flying simultaneously, and shall hence be called the low flyer (52.004) and high flyer (52.003), with respect to their altitudes. The rockets were launched on December 8th, 2018 from Andøya Space Center in Andøya, Norway, located at 69°17' N, 16°01' E. The high flyer was launched at 08:26:00 UT and reached its apogee at 1042.2 km at 08:37:16 UT or 676 s after launch. The low flyer was launched at 08:28:00 UT and reached its apogee at 756.8 km at 08:37:46 UT or 586 s after launch.

### 2.2 Multi-Needle Langmuir Probe (m-NLP)

We used data from the multi-needle Langmuir probe (m-NLP), which can be used to calculate the electron density with very high sampling rates. For a set of cylindrical probes, the electron density  $n_e$  can be acquired from

$$n_e = \left( \frac{m_e}{2e(2erl)^2} \frac{d(I_c^2)}{dV} \right)^{\frac{1}{2}}, \quad (1)$$

where  $m_e$  is the electron mass,  $e$  the elementary charge,  $r$  and  $l$  the probe radius and length, respectively,  $I_c$  the current collected by a single probe, and  $V$  the respective probe bias (Jacobsen et al., 2010; Bekkeng et al., 2010). The factor  $\beta = 1/2$  is for an infinitely long, cylindrical probe, thus if the squared currents drawn to each probe are plotted against the corresponding probe biases, the electron density can be obtained from the slope of a line in this plot. For a probe deviating from this geometry, the factor differs from  $\beta = 1/2$  (Marholm & Marchand, 2020). The obtained electron density for a probe with  $\beta = 1/2$  is then independent of the spacecraft potential and the electron temperature. However, for  $\beta \neq 1/2$ ,  $n_e$  may be affected by changes in the floating potential and temperatures. The absolute density obtained with a  $\beta \neq 1/2$  has been observed to be off by 20–45% compared with  $\beta = 1/2$ , while simulations have found an overestimation of the density by up to an order of magnitude (Hoang et al., 2018; Guthrie et al., 2021).

Both rockets used in this work were equipped with one probe system each, which consisted of four cylindrical probes with a diameter and length of 0.51 mm and 39 mm, respectively. The probes allowed to calculate the electron density at a sampling rate of 10 kHz using probes with fixed biases of 3 V, 4.5 V, 6 V, and 7.5 V. The probes were mounted in a cross-like formation perpendicular to the spacecraft axis with a distance of 1 m between oppositely mounted probes.

In addition to the m-NLP, we present data from the DC electric field instruments (DC E), an on-board magnetometer, and the Energy and Pitch Angle Analyzer (EEPAA) on both rockets and 557.7 nm and 630 nm emission lines from the all-sky imager (ASI) which is based in Ny Ålesund, Norway. The ASI was calibrated at the UNIS calibration lab in Longyearbyen in January 2013. Further information about the brightness and orientation calibration is given on the ASI data page of the University of Oslo.<sup>1</sup>

The DC E is composed of four spherical probes in a similar formation as the m-NLP with a distance of 6.5 m between two opposing probes, the probes were able to measure the electric field with a cadence of 2.5 kHz. The filtered data used is in geographic coordinates and was filtered with a lowpass Butterworth filter at 1 Hz. The magnetic field was measured by a magnetometer that measured the three-axis magnetic field components for the duration of the flight in geographic coordinates. We assume both measurements to have an error of around 5%, which arises due to uncertainties in the geometries, the deployment of the instruments, and noise. The EEPAA consisted of several detectors mounted in 10° steps around the spacecraft axis, where 0° corresponded to the upward direction. We used the 0° data from the EEPAA, which shows the electrons precipitating downwards along the magnetic field lines.

### 3 Observations

Measurements of the interplanetary magnetic field show a steady negative  $B_z$  of  $\approx -5$  nT prior to launch (Moser et al., 2021). The background auroral observations can be seen in Figure 1, which shows the ASI data for the 630 nm (upper row) and 557.7 nm (lower row) emission from Ny Ålesund at different times while the rockets were intersecting the cusp region. The data were projected onto a height of 250 km for the red (630 nm) and 150 km for the green (557.7 nm) emission line. The green and dark blue for the upper panel and orange and magenta lines lower panel indicate the trajectories and the colored triangles and squares for the low and high flyers, respectively, show the current position of the rockets. The trajectory of the high flyer is the left trajectory, and the low flyer trajectory is the right trajectory. The black arrows protruding from the trajectories in the two left panels show the electric field vector in the  $E_E$ - $E_N$ -plane in geographic coordinates taken from the DC E instrument with a cadence of 2.5 kHz. The arrow lengths show the magnitude of the electric field in arbitrary units but are both scaled with the same factors, and the length can therefore be taken as an indicator of the field strength. For visibility reasons, the electric field for the high flyer is only depicted in the upper

panel, while the field vectors for the low flyer are only depicted in the lower panel. While it was partly cloudy, it can be seen that both flyers were launched into dayside aurora and intersected the cusp regions, which are dominated by red emission. The high flyer entered the cusp around 08:35 UT and the low flyer around 08:37 UT. The rockets exit the region again towards the end of the flight. The electric field vectors show a mostly westward electric field for both rockets with a growing northward component for the low flyer until the rockets enter the cusp, where the field abruptly changes to a south-eastward direction and intensifies.

Figure 2 shows the electron densities and detrended electron densities of the high and low flyer, respectively, obtained from the m-NLP. For the calculation of the electron density, the spin frequency and harmonic frequencies were removed using band-pass filters. The data was then detrended using a 5th-order Savitzky-Golay filter with a 3-second interval. Note that two intervals in each panel are marked in transparent blue. Due to attitude changes of the rockets, the data collected in these intervals includes artificial spikes in density fluctuations. These transparent overlays will be used for all data sets derived from the density in this work. The electron density for the high flyer (Fig. 2a) shows values between 2 and  $9 \times 10^9 \text{ m}^{-3}$  with peaks starting around 08:35 UT and ending around 08:39:30 UT. The detrended density for the high flyer (Fig. 2b) shows fluctuating values up to  $3 \times 10^9 \text{ m}^{-3}$ , with small fluctuations up until 08:37 UT and larger fluctuations until 08:39:30 UT. The electron density for the low flyer (Fig. 2c) shows higher densities between  $4 \times 10^9 \text{ m}^{-3}$  and  $2 \times 10^{10} \text{ m}^{-3}$  with two peaks around 08:38 UT and 08:40 UT with densities up to 1.5 and  $2 \times 10^{10} \text{ m}^{-3}$ , respectively. The detrended density (Fig. 2d) shows fluctuating values up to  $5 \times 10^9 \text{ m}^{-3}$  with smaller fluctuations until 08:35:30 UT followed by stronger fluctuations until 08:42 UT.

In order to analyze the electron density fluctuations, the detrended density was Fourier transformed using the Fast Fourier Transform (FFT) and a Hanning window with intervals of 2 s each, which corresponds to 20,000 collected samples and to a flight distance up to 8 km, and an overlap of 50% for the windows. Typical power spectra obtained for these intervals plotted in log-log scale can be seen in Figure 3 in the bottom panels. The figure also shows the current collected by each of the Langmuir probes (upper panels) and the corresponding detrended electron density (middle panels). For each 2 s interval, we analyzed if the best fit was one or two straight lines and, in the latter case, at which frequency the spectral break occurred. The fitting was done using a first-order polynomial fit on log-log axes. The start and end points of the fitted interval and a possible break point were first chosen through manual iteration of possible values to get a frequency range in which breakpoints occur. Afterwards, the start, break, and endpoints were chosen from a range of frequencies deemed possible for each of the points. The ranges for each point were between 1 Hz and 10 Hz, between 20 Hz and 100 Hz, and 120 Hz and 250 Hz for the start, break, and endpoints, respectively. The points were chosen by a loop of iterations over the possible frequencies. Then it was examined if the slopes of the two fits were deviating by more than 0.8, and if the low-frequency (LF) slope  $p_1$  had a lower absolute value than the high-frequency (HF) slope  $p_2$ . If this was the case, the power spectrum was considered to show a double slope. If the deviation was smaller

<sup>1</sup> All-Sky Imager Data from Ny Ålesund, Svalbard, University of Oslo, <http://tid.uio.no/plasma/aurora/tech.html>, Date accessed: 2022-11-29.

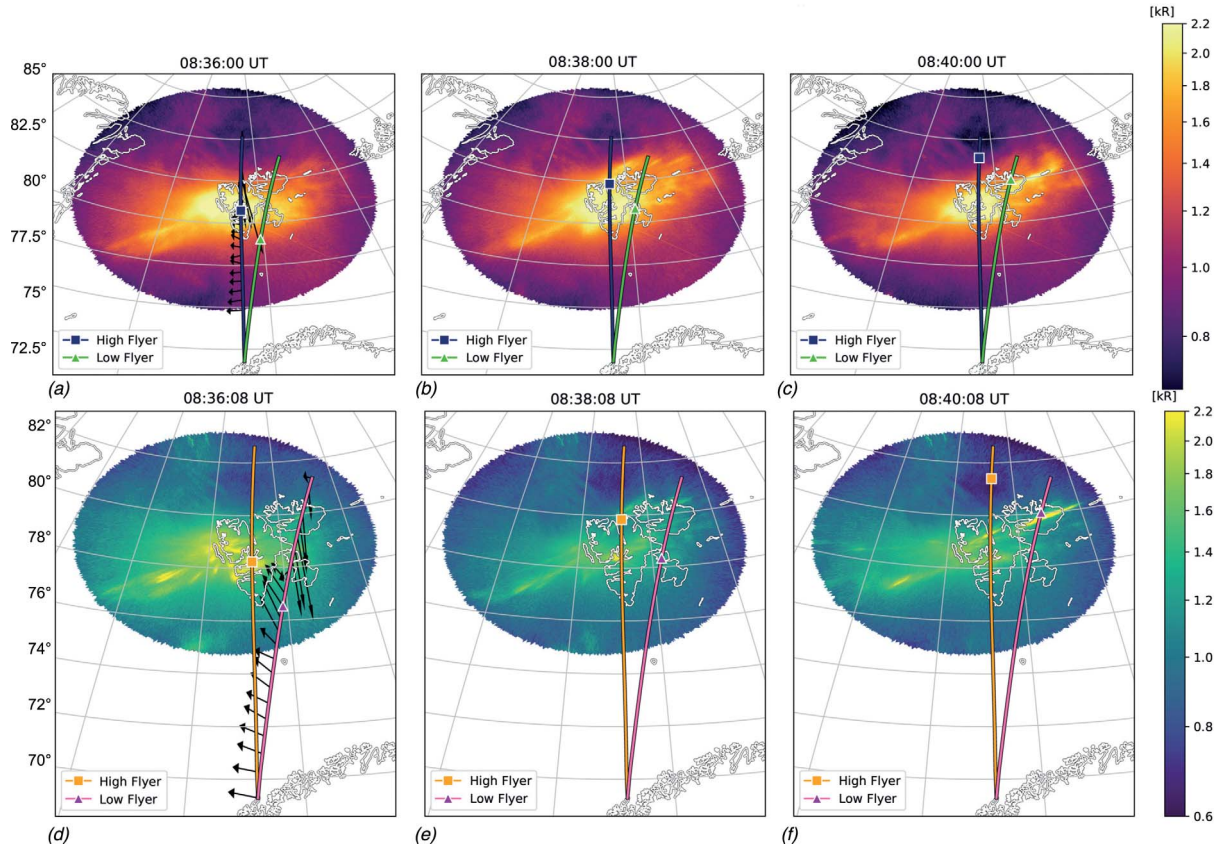


**Figure 1.** 630 nm (upper row) and 557.7 nm (lower row) All-Sky Imager Data from Ny Ålesund projected to 250 km at 08:36 UT (a), 08:38 UT (b), and 08:40 UT (c) for the 630 nm emission, and projected to 150 km at 08:36 UT (d), 08:38 UT (e), and 08:40 UT (f) for the 557.7 nm emission; the rocket trajectories are shown in dark blue and orange for the high flyer and in green and magenta for the low flyer, respectively. A filled square and filled triangle is indicating the current position for the high and low flyer, respectively. The black arrows indicate the electric field vector obtained from the DC E for the high flyer (upper left panel) and the low flyer (lower left panel).

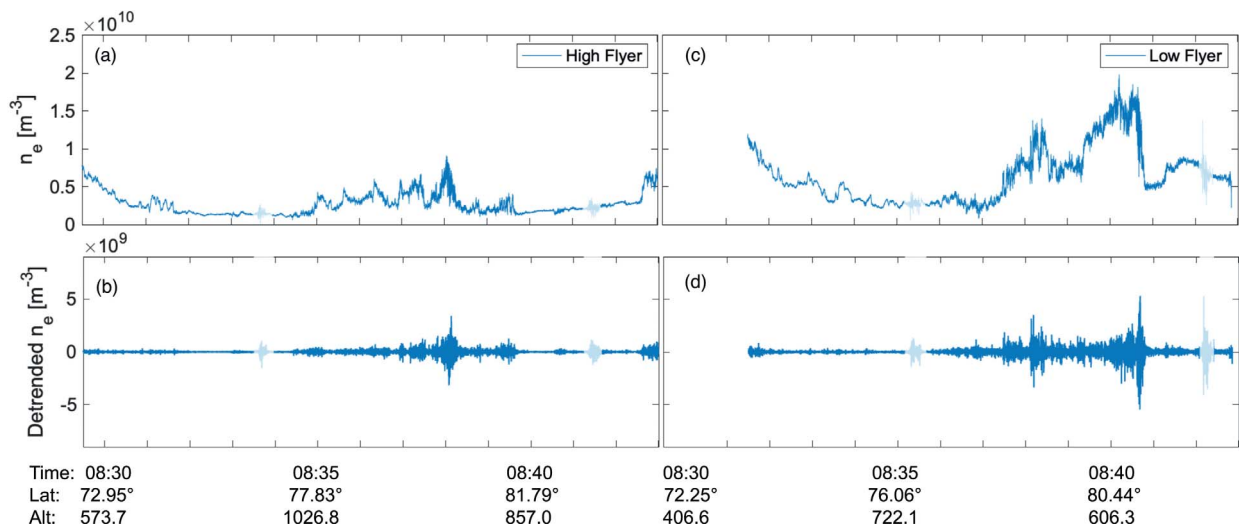


**Figure 2.** (a) Electron density of the high flyer measured with the m-NLP, (b) detrended electron density of the high flyer, (c) electron density of the low flyer, measured with the m-NLP, (d) detrended electron density of the low flyer; the density was detrended using a 5th-order Savitzky-Golay filter. The transparent data intervals correspond to attitude changes of the spacecraft. The x-axes correspond to UT (upper line), the magnetic footprint of the spacecraft (middle line), and the altitude of the rocket (bottom line).

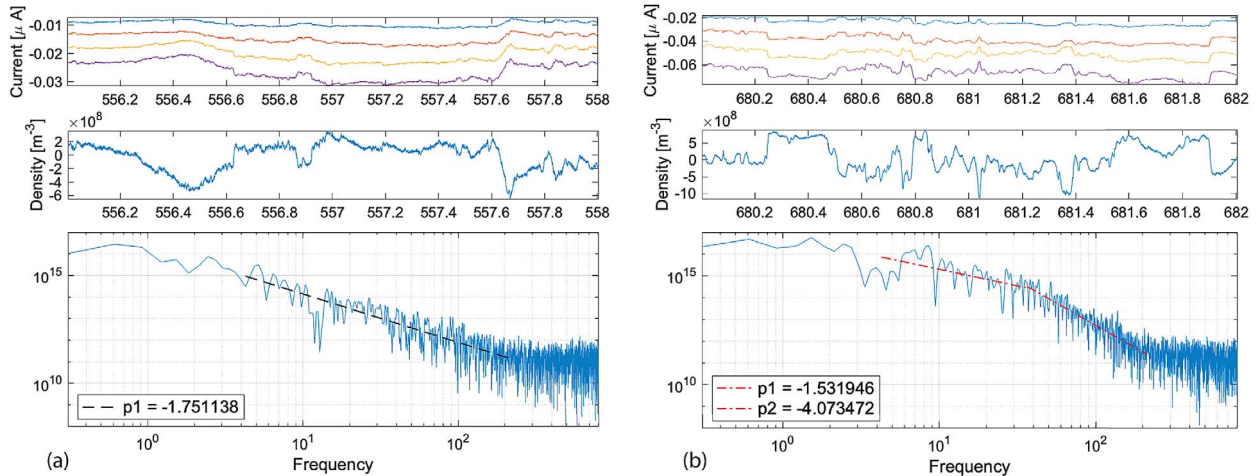


**Figure 3.** Detrended electron density obtained from the m-NLP, and the corresponding power spectrum for the flight interval between 556 s and 558 s (a) and 680 s and 682 s (b) of the low flyer. The bottom panel in (a) shows a power spectrum with a single slope of  $p = -1.97$ , while the bottom panel in (b) shows a power spectrum fitted with two slopes  $p_1 = -1.64$  and  $p_2 = -4.10$ .

than 0.8 the spectrum was best described by a single slope.  $|p_1| + 0.8 \leq |p_2|$  was found to be a good condition to distinguish between a double and single slope fit and was used as a condition in previous works (Ivarsen et al., 2021). Figure 3a shows the power spectrum of the low flyer at 08:37:16–08:37:18 UT, which corresponds to a time shortly after the rocket entered the cusp. This power spectrum was best described by a single slope fit calculated to be  $p_1 = -1.97$ . Figure 3b shows the power spectrum of the low flyer at 08:39:20–08:39:22 UT, which corresponds to the rocket being in the middle of the auroral region. This power spectrum exhibited a spectral break at  $f \approx 38$  Hz and was thus best described by two different first-order fits calculated to be  $p_1 = -1.64$  and  $p_2 = -4.10$ .

In order to analyze the entire flight and compare data from different instruments, Figure 4 shows the data obtained from the high flyer (left) and low flyer (right). For completeness, Figures 4a and 4b show the detrended electron density for the flight duration (compare Fig. 2). Figures 4c and 4d show the corresponding spectrograms obtained with an FFT and a Hanning window using 20,000 data points, which corresponds to 2 s intervals. The spectrogram shows the frequency range 15–1000 Hz. It can be seen that a high PSD up to 1000 Hz is reached in distinct areas corresponding to the electron density fluctuations mentioned above for both rockets. The white crosses show the frequencies of the spectral knee of the corresponding power spectrum, where a double slope fit was best to fit the spectrum. A clear connection between strong electron density fluctuations and the appearance of a double slope can be seen and generally, the power spectra of the low flyer show more double slopes compared to the high flyer. The spectral breaks for both rockets are located between 20 Hz and 105 Hz. While the highest frequencies are around 90 Hz or 100 Hz, the median spectral break for high and low flyers are located at  $f_{\text{HighFlyer}} \approx 45$  Hz and  $f_{\text{LowFlyer}} \approx 46$  Hz, respectively. The spectral break at around 08:33:30 UT in Figure 4c falls into the transparent interval indicating the attitude change and could therefore be artificial. Note also that the spectrogram does not show values below 15 Hz. The low flyer showed one spectral break below 15 Hz, which is thus not depicted in this figure.

For the low flyer the spectral break frequency exhibits a local maximum of  $\approx 80$  Hz at around 08:38:00 UT and a global maximum of  $\approx 104$  Hz at roughly 08:40:00 UT. Then the occurrence of double slopes abruptly stops for about half a minute, until at around 08:41:00 UT when the rocket encounters another small region of double slopes. Then, for the rest of the flight, the power spectra only exhibit single slopes. For the high flyer, the spectral break frequencies exhibit one maximum of  $\approx 100$  Hz at roughly 08:38:00 UT, similar to the first maximum of the low flyer. While the occurrence of double slopes more or less abruptly stops around 08:40:00 UT, a region with double slopes exists at the very end of the flight, exhibiting very large discrepancies in their fitted slopes (see Fig. 4e). Figures 4e and 4f show the HF and LF slopes for the fit of the power spectra in blue and red, respectively. If only the HF slope is seen with no corresponding LF slope, a single slope was detected. The median slopes for the high and low flyers, respectively, were found to be  $-1.83$  and  $-1.85$  for the low-frequency slope and  $-3.03$  and  $-3.07$  for the HF slope. The median for the single slope spectra is  $-1.98$  and  $-2.08$  for the high and low flyers, respectively. While for the high flyer, the slopes seem to fluctuate around  $p = -2$ , with no larger intervals of consecutive double slopes, the low flyer shows larger regions, where several double slopes are detected in a row, see Figure 4f between 08:38 and 08:39 UT and around 08:40 UT. The appearance of a double slope naturally coincides with the spectral breaks seen in the previous Figures 4c and 4d. The appearance of double slopes and thus, spectral breaks rises with the beginning of electron precipitation (see Figs. 4k and 4l), but does not subside right after the rockets leave the auroral region.

In addition to the slope of the fitted power spectrum, we investigated the power associated with different frequency regimes for each power spectrum, in order to understand how the power is distributed in the different frequency bands at different altitudes. For this, we integrated the power spectra with respect to frequency. Figures 4g, 4h, 4i, and 4j show the normalized integrated power spectra for 10 Hz and 100 Hz intervals, respectively. For each power spectrum, the power was integrated for 10 Hz intervals between 10 Hz and 100 Hz

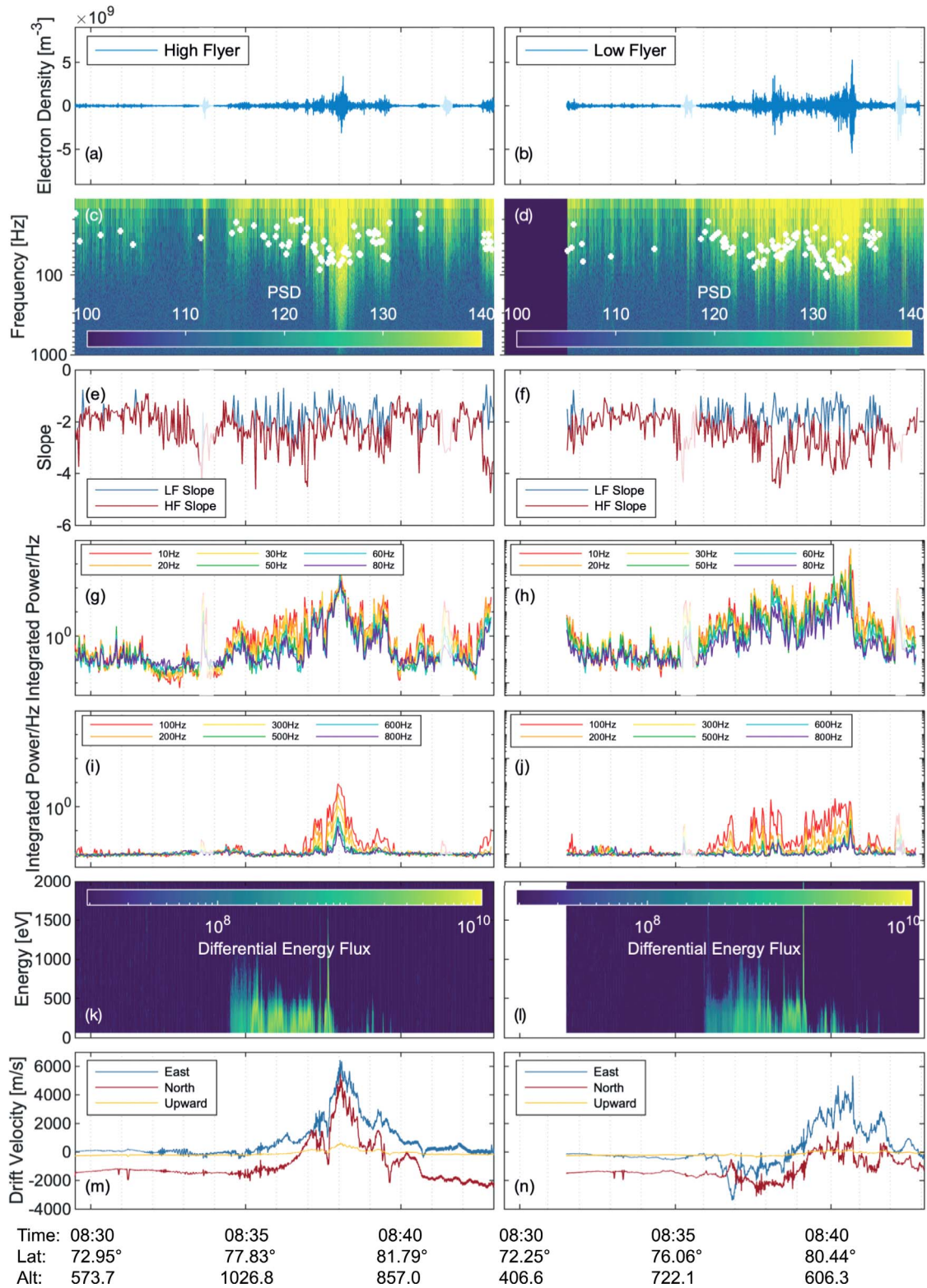


**Figure 4.** Detrended  $n_e$  (a, b), PSD of the m-NLP  $n_e$  fluctuations with the spectral break frequency (c, d), LF and HF slopes of the corresponding PSD (e, f), integrated power from the PSD for frequency intervals of 10 Hz (g, h) and for intervals of 100 Hz (i, j), electron precipitation measured with the EEPAA (k, l)  $E \times B$ -drift velocity  $v_D$  in ENU-coordinates (m, n) of the **high flyer** and **low flyer**, respectively. The transparent data intervals correspond to attitude changes of the spacecraft. The x-axes correspond to UT (upper line), the magnetic footprint of the spacecraft (middle line), and the altitude of the rocket (bottom line).

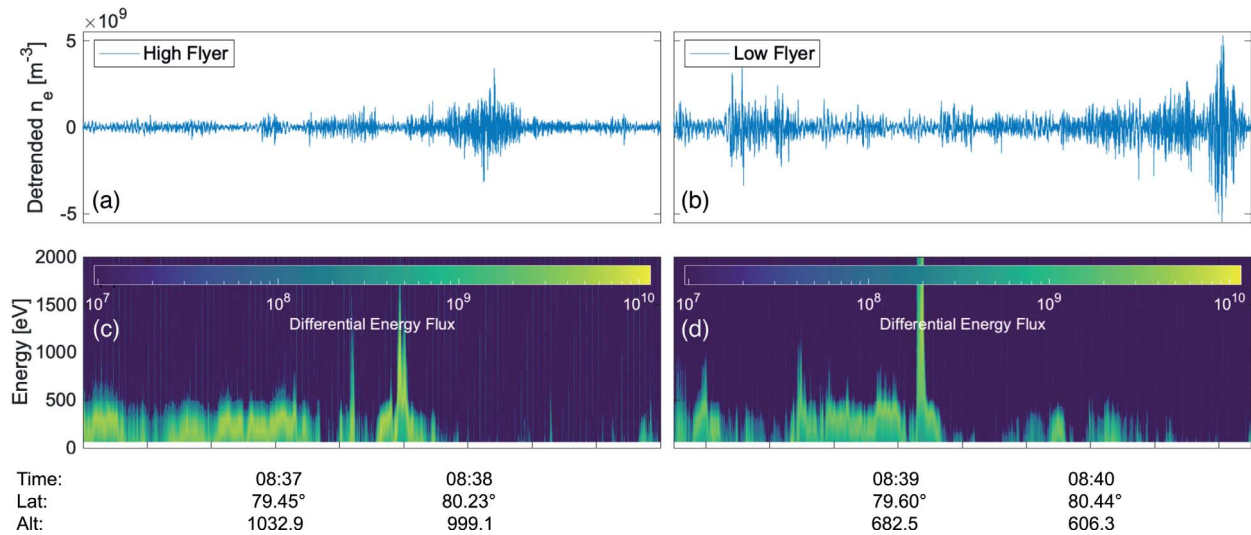


**Figure 5.** Detrended electron density and electron precipitation of the high flyer (a, c) and the low flyer (b, d) between 08:36:30 and 08:39:00 UT and between 08:38:00 and 08:41:00 UT, respectively. The x-axes correspond to UT (upper line), the magnetic footprint of the spacecraft (middle line), and the altitude of the rocket (bottom line).

(Figs. 4g and 4h), and 100 Hz intervals between 100 Hz and 1000 Hz (Figs. 4i and 4l). The values were then normalized with two different factors. The first factor was the length of the integration interval, which was 10 Hz for Figures 4g and 4h and 100 Hz for Figures 4i and 4j. This was done in order to normalize power to power per Hz, so all four panels could be compared in an easier manner. As the power in the spectrum falls off, naturally intervals with lower frequencies have higher powers. In order to compare all frequency intervals with each other, the intervals were normalized by a median power value which was obtained from the whole flight duration used. The normalization factors for each frequency interval for both flyers and a detailed description of the normalization process can be seen in Table A1 in Appendix.

As seen in Figures 4g and 4h, the integrated power at frequencies between 10 Hz and 100 Hz shows similar relative fluctuations, but overall more elevated power with more fluctuations throughout the flight, especially while the rocket is flying through the cusp. While for the low flyer, the power rises for all frequencies, the high flyer shows a rise in power mainly in the lower frequencies. The frequency intervals between 100 Hz and 1000 Hz behave differently (Figs. 4i and 4j). For the high flyer (Figs. 4i) the strongest relative fluctuations are found right after particle precipitation ends at 08:38:00 UT (Fig. 4k), which shows the differential energy flux of precipitating electrons) and coincide with entering a flow channel (see Fig. 4m showing the  $\mathbf{E} \times \mathbf{B}$ -drift velocity in ENU-coordinates). Outside of that time interval, there are hardly any fluctuations seen for intervals above 100 Hz. For the low flyer (Fig. 4j), the 100 and 200 Hz frequencies are enhanced much stronger than frequencies between 300 Hz and 1000 Hz the strongest fluctuations exist between 08:36 UT and 08:41 UT. While some of the peaks in integrated power fall into regions with little detected particle precipitation, the overall region where the integrated power is elevated coincides well with electron precipitation and, similar to the high flyer, the immediate region afterwards. Additionally, the integrated power

of the low flyer correlates with a change in electric field and a change in particle velocity, especially for the second rise of integrated power around 08:39 UT.

Figures 4k and 4l show the electron particle precipitation for the high and low flyers, respectively. For the high flyer, the precipitation starts around 08:34:30 UT with values up to 1000 eV which drops to around 500 eV roughly a minute later. The region of precipitation ends around 08:38:00 UT, except for a few low energetic detected particles around 08:39:00 UT. Precipitation for the low flyer starts at 08:36:00 UT with energies around 500 eV and raises to energies around 1000 eV at 08:37:00 UT. The region of precipitation lasts until about 08:39:00 UT, and just like the high flyer, small regions with low energetic precipitation show up until 08:41:30 UT. Both the high and low flyer have precipitation gaps in the regions of strongest precipitation, and just before the rocket leaves the regions, a strong, thin peak is found with energies up to 2000 eV for the high flyer and 4000 eV for the low flyer. Figures 4m and 4n show the  $\mathbf{E} \times \mathbf{B}$ -drift velocity in ENU-coordinates for the high and low flyer, respectively. The drift velocity was calculated from the DC  $E$  instrument and the magnetometer on board each of the rockets. As the magnetic field and electric field measurements were not taken at the exact same time, the magnetic field was interpolated to estimate the magnetic field values at the time the electric field was obtained. Due to the high cadence and thus low distance between the measurement points, the interpolation was one using a first-order polynomial between each point. The drift velocity was then obtained from  $\mathbf{v}_D = \mathbf{E} \times \mathbf{B}/B^2$  the drift velocity for the high flyer (Fig. 4m) shows a southward flow of around  $1.5 \text{ km s}^{-1}$  with a small eastward component. At about 08:36:00 UT the flow turns into the north-east directions with a drift velocity up to  $7 \text{ km s}^{-1}$  which is reached at 08:38:00 UT. Afterwards, the flow goes back into the original southeast direction with a velocity of  $2 \text{ km s}^{-1}$  for the rest of the flight. The drift velocity for the low flyer starts similar to the high flyer with a southward flow of around  $1.5 \text{ km s}^{-1}$ . The direction of flow turns southwest around

08:36:30 UT and then changes to an eastward flow with peaks between 08:40:00 and 08:41:00 UT with a velocity of roughly  $6 \text{ km s}^{-1}$ . Afterwards, similarly to the high flyer, it goes back to the original direction and speed.

Figure 5 shows the detrended electron density and the electron precipitation for the high and low flyer. The strongest electron density fluctuations can be seen around 8:38:00 UT for the high flyer and around 08:40:40 UT for the low flyer. The low flyer also exhibits density fluctuations around 08:38 UT. It can be seen that there is a correlation between high electron density fluctuations and low detected precipitation and the largest density fluctuations happen right after the rockets leave the auroral region.

## 4 Discussion

Irregularities can occur in the ionosphere when free energy is introduced into the system and is then redistributed over a variety of scales until the free energy is dissipating on small spatial scales. One source of free energy in the ionosphere is the influx of energetic particle precipitation (Kelley et al., 1982b; Moen et al., 2002, 2013).

The TRICE-2 sounding rockets encountered energetic electrons at different altitudes. In order to analyze fluctuations in the electron density, power spectra were made for both flights. It has been shown that power spectra of plasma fluctuations in the high-latitude ionosphere display a steeper slope for higher frequencies if plotted logarithmically (Villain et al., 1986; Basu et al., 1990; Spicher et al., 2014; Ivarsen et al., 2019; Di Mare et al., 2021). We found that a double slope for the PSD started appearing at the same time that both the high and low flyers entered the region where particle precipitation was encountered. While particle precipitation seems to in a way trigger the presence of double slopes, the overall distribution of their appearance and the corresponding spectral break frequency does not seem to follow the precipitation. Instead, the frequency of the break in the double slope seems to follow the magnitude of the measured electric field. While the frequencies of the spectral breaks fall between 20 and 105 Hz, the largest values are reached when the electric field also reaches its maximum. This holds true for both the high and low flyers. While the appearance of double slopes seems to coincide with the beginning of precipitation, there are still double slopes found minutes after the rocket leaves the auroral region again, though the rate of occurrence lessens. The low flyer shows a gap around 08:41 UT for about half a minute where no double slopes are detected before another set of double slopes is found. While there are no double slopes registered at the end of the flight interval for the low flyer, the high flyer exhibits an increase of double slopes with a very steep  $p_2$ . This corresponds to a region where the rocket encounters a highly structured plasma with an increased density far into the polar cap. The appearance of double slopes during strong electron density fluctuations is in accordance with earlier measurements (Spicher et al., 2014; Ivarsen et al., 2019; Di Mare et al., 2021).

The median values of the LF and HF slopes are  $-1.83$  and  $-3.03$  for the high flyer and  $-1.85$  and  $-3.07$  for the low flyer, respectively. These slopes are in accordance with earlier results that found an LF slope of  $\approx 5/3$  and an HF slope between 3 and 5 (Villain et al., 1986; Basu et al., 1990; Spicher et al., 2014;

Ivarsen et al., 2019; Di Mare et al., 2021). The median frequencies of the spectral breaks are found to be around 45 Hz for both rockets and are reasonably close and could correlate to the oxygen gyrofrequency found at these heights, which are between  $\omega_{\text{HighFlyer}} \approx 33\text{--}38 \text{ Hz}$  and  $\omega_{\text{LowFlyer}} \approx 39\text{--}45 \text{ Hz}$  for the main duration of the flights for the high and low flyer, respectively. However, the frequencies of the spectral breaks have been observed for decades and found at several different frequencies, thus it is difficult to assume the physical meaning behind the break frequency. The rise in spectral break frequency along with the rise in electric field magnitude or drift velocity can be due to a Doppler shift correlated to the large drift velocity. When the drift velocity rises, the power spectra can be shifted to higher frequencies for the observer, which results in a higher frequency of the spectral break. This is consistent with Spicher et al. (2022), who showed that small-scale structures were convected with the  $\mathbf{E} \times \mathbf{B}$  flow.

Particle precipitation is believed to be an important source of large-scale irregularities, and we found that for both rockets the strongest electron density fluctuations were in regions just outside electron precipitation, thus poleward of the cusp, or in regions with low detected electron precipitation.

Additionally, a lot of enhancements in the electron density fluctuations fall into gaps of particle precipitations. In regions of strong particle precipitation, a strong E-region conductivity can result in a channel between the E- and F-region, where electrons can move between the regions. It was found that in the case of a strongly conducting E-region, the electrons lead to a faster decay in electron density irregularities in the F-region (Kelley et al., 1982b; Basu & Coppi, 1988; Takahashi et al., 2022). Enhancements in conductivity below the rockets could thus explain the stronger electron density fluctuations in regions where no or very little precipitation was detected. Note, that while low precipitation seems to coincide with higher density irregularities, there are no enhanced density fluctuations in regions southward of the cusp.

Another explanation for increased electron density fluctuations poleward of the cusp could be that particle precipitation is structuring the plasma within the cusp. This leads to the convection of the structured plasma poleward out of the cusp into the polar cap. Due to the relative movement of the structured density patch through the background plasma in the polar cap, this movement can then be responsible for an increase in irregularities just beyond the cusp, for example, the GDI (Carlson et al., 2007; Moen et al., 2013). Spicher et al. (2014) have found the largest fluctuations in electron density irregularities for the low flyer poleward of the cusp. We can now also show that this is the case for the high flyer as well.

In addition to an analysis of the slopes in the power spectra, we looked at integrated power in order to understand in which frequency interval the most and least power exist. For frequencies between 10 Hz and 100 Hz, the relative fluctuations in integrated power are uniformly elevated throughout the flight for both flyers, however, they show a raise in a region with precipitation. While the low flyer shows a rise in power for all frequencies, the power for the high flyer rises mainly in the lower frequencies between 10 Hz and 30 Hz during the period when the rocket encounters particle precipitation. This could show that energetic particle precipitation is depositing energy into lower frequencies, where the free energy can be used to further structure the plasma.



While the power for the low frequencies is elevated more evenly, especially within regions of precipitation, there is a difference at higher frequencies. For the high flyer, there are few fluctuations throughout the flight, except a spike around 08:38 UT, which occurs immediately after the rocket leaves the region where electron precipitation is detected. This spike coincides with a large change in the electric field and thus a strong increase in the drift velocity corresponding to a flow channel. The strong rise in fluctuations at 08:38 UT occurs in all frequency intervals between 100 Hz and 1000 Hz.

The low flyer data show strong fluctuations in the integrated power between 08:36 UT and 08:41 UT. This mainly coincides with the strong rise in the electric field and the corresponding drift velocity, similar to the high flyer. While the high flyer data show a strong correlation between electric field and integrated power, however, the integrated power for the low flyer deviates slightly from the drift velocity measurements. While the region of elevated power starting around 08:39 UT correlates with a rise in drift velocity up to  $6 \text{ km s}^{-1}$ , the first region of elevated power starting around 08:37 UT shows nearly the same elevation in integrated power as the second elevation region does, but the drift velocity only raises to about 1/2 of the velocity of the second interval. Additionally, the low flyer exhibits another rise in integrated power before the other two intervals, starting around 08:36 UT, which falls together with the beginning of particle precipitation and a momentary change of drift velocity in the western direction. It seems that similar to the electron density fluctuations, peaks of the integrated power seem to fall into gaps in the precipitation. This becomes especially obvious for the double peak in power observed for the low flyer starting right after 08:38 UT which falls exactly into a double gap of precipitation at the same time. This again can be explained with a quenching of instabilities due to a highly conducting region below the rocket, similar to the explanation of the occurrence of electron density fluctuations.

Important to notice that, while the high flyer shows a rise in integrated power in all frequency intervals, the low flyer mainly exhibits a rise in power in the frequency range below 200 Hz. The integrated power of the high flyer agrees with the change in drift velocity while the integrated power of the low flyer only agrees to a certain degree, and could partially depend on the onset of precipitation similar to the lower frequencies. Thus, there is a possibility that plasma density irregularities are driven by different mechanisms at different altitudes.

For the purpose of this paper, we were interested in changes in the electron density with respect to precipitating particles and changes in the plasma drift. As described in [Section 2](#), we estimate the error of both the electric and magnetic field instruments to be around 5%, which arises due to uncertainties mainly in the geometry and due to noise. While noise is affecting very small or fast signals, we only look at the overall trend in the drift velocity. Thus, we assume that noise has little effect on our results. The error in the geometry has been minimized by repeatedly deploying the booms before launch and measuring that the booms are in fact pointed in the direction they should. The distance between the booms was measured accurately to about a cm, while the direction was measured to an accuracy of about arc seconds of a degree. With a distance of 3 m per boom, these lead to errors that are smaller than 1%. Additionally, slight inaccuracies in the orientation of the probes towards the magnetic field may lead to uncertainties when calculating

the electric field. As these errors are again small, we estimate the total error to not be bigger than 5% in total for both magnetic and electric field measurements. The key finding obtained from relating the spectra and the drift velocity is a rise in the frequency of the spectral break with increased velocity, which is unaffected by the errors mentioned above. For the errors in the electron density, we know the error in the sampling of the currents drawn to the m-NLP to be of the order of nA, which results in errors in density due to measurement uncertainties of less than a percent. Our main analysis tool in this work is the use of power spectra which are taken from 20,000 data points in 2-second intervals, and we used a Hamming window with 50% overlap to reduce the effect of taking a specific time interval for the spectrum. Additionally, smaller uncertainties in the spectra for frequency ranges at both ends of the power spectra are being considered. As we assume that all four probes in the mNLP system are measuring the same plasma at the same time, the high frequencies in the spectra may be affected for those higher than the frequency corresponding to the distance between the probes and the speed of the rocket. With a distance between the probes of 1 m, and assuming an average speed of the rocket of  $3 \text{ km s}^{-1}$ , spectral components below about 350 Hz should not suffer large errors from calculating the electron density with this inter-probe separation. On the other hand, the low-frequency side of the spectrum may be prone to errors due to the spin of the rocket and influenced by the detrending process. We have removed the spin frequency of around 0.6 Hz and harmonics with band-pass filters. As the detrending process was done with a Savitzky-Golay filter, the frequency may vary but should not reach more than 2 Hz. However, as we only use values between 3 Hz and 300 Hz for the analysis of the slope, these should have a minor impact. The last error we shall consider is the uncertainty that comes from  $\beta = 0.5$ . This error has been estimated to be 25–40% ([Hoang et al., 2018](#)), while simulations showed deviations of up to an order of magnitude ([Guthrie et al., 2021](#)). We are mainly interested in the relative fluctuations of the density and not in absolute densities, thus systematic uncertainties that lead to an overall over- or underestimation of the density are not crucial for the work in this paper ([Marholm, 2020](#)). Furthermore, we try to counter uncertainties in the electron density PSD by using overlapping windows for the Fourier transform of 50% and takes a large sampling size for each spectrum of 20,000 sampling points. If there are uncertainties in the electron density, it may shift the spectrum for certain frequencies. As we do not try to make an analysis by quantifying the slopes in detail but rather analyzing the trend of the slope and integrated power with respect to precipitating electrons and drift velocity, we assume the uncertainties due to the measurement of the electron density do not alter any of the main points discussed in this paper.

## 5 Conclusion

In this work, we show that particle precipitation in the cusp ionosphere is of importance for the formation of large-scale irregularities. Electron density fluctuations and the corresponding power spectra obtained from both rockets in the TRICE-2 campaign were analyzed. The largest fluctuations in the electron density were found in regions immediately after the rockets left

the region of precipitation, thus poleward of the cusp. Strong electron density fluctuations fall into gaps of detected precipitation. This could be due to a higher conductance below the rockets resulting from energetic particle precipitation which leads to a faster decay of irregularities in the F-region. Another reason may be that the rocket encounters structured plasma that travels poleward out of the cusp into the polar cap, where the relative movement of the high-density plasma gives rise to instabilities.

Furthermore, we found that the power spectra in the cusp region were best described by a double slope. We found frequencies for the break frequency of the slope that may coincide with the oxygen gyrofrequencies at these altitudes. Shifts of the break frequency to higher frequencies are correlating with a rise in the  $\mathbf{E} \times \mathbf{B}$ -drift velocity. This correlation could be due to a Doppler shift, moving the power spectrum up to higher frequencies. The break frequencies have been analyzed for decades and have been found at several different scales, thus making a physical explanation difficult. In addition to the slopes of the power spectra, we also analyzed the relative integrated power in different frequency intervals. For low frequencies, the whole flight interval is elevated with larger fluctuations throughout the flight for both rockets. This elevation is pronounced specially for regions of particle precipitation, suggesting that precipitation deposits energy into larger scales. For higher frequencies, the integrated power for the high flyer is quiet for most of the flight, except for a sharp peak right after the rocket left the cusp, which correlates to a large peak in drift velocity. The high-frequency integrated power for the low flyer is enhanced for a longer time interval. While it mostly overlaps with a rise in drift velocity, it is not proportional as seen for the high flyer, and the integrated power starts rising with an onset of precipitation, before the drift velocity changes. This could indicate that different mechanisms are dominant at different altitudes. For further studies on how particle precipitation influences the formation of irregularities, it would be beneficial to examine these results statistically for longer periods of time and a larger range of altitudes.

**Acknowledgements.** The m-NLP experiment and the University of Oslo (UiO) participation in the Grand Challenge Initiative Cusp rocket campaign were funded through the Research Council of Norway (RCN) grant 275653. The authors thank Espen Trondsen, David Michael Bang-Hauge, and the Mechanical Workshop at UiO for the m-NLP instrument. This work was partially conducted within the 4DSpace research initiative at UiO. The study was supported in part by the European Research Council (ERC) under the European Union's Horizon 2020 research and innovation program (grant agreement No 866357). Data from the TRICE-2 missions can be found at: [https://phi.physics.uiowa.edu/science/tau/data0/rocket/SCIENCE/TRICEII\\_Mission/](https://phi.physics.uiowa.edu/science/tau/data0/rocket/SCIENCE/TRICEII_Mission/). The authors thank the Andøya Space Center for launch operations, KHO/UNIS/UiO for support with ground-based observations, and all the personnel involved in the mission. S.M. acknowledges Øyvind Jensen and the Institute for Energy Technology (IFE) for permission to see this work through to the end while at IFE. A.S. acknowledges funding from RCN grant 326039. The editor thanks P. Thayyil Jayachandran and Weijia Zhan for their assistance in evaluating this paper.

## References

- Basu B, Coppi B. 1988. Fluctuations associated with sheared velocity regions near auroral arcs. *Geophys Res Lett* **15**(5): 417–420. <https://doi.org/10.1029/gl015i005p00417>.
- Basu S, Basu S, MacKenzie E, Coley W, Sharber J, Hoegy W. 1990. Plasma structuring by the gradient drift instability at high latitudes and comparison with velocity shear driven processes. *J Geophys Res Space Phys* **95**(A6): 7799–7818. <https://doi.org/10.1029/JA095iA06p07799>.
- Bekkeng T, Jacobsen K, Bekkeng J, Pedersen A, Lindem T, Lebreton J, Moen J. 2010. Design of a multi-needle Langmuir probe system. *Meas Sci Technol* **21**(8): 085903. <https://doi.org/10.1088/0957-0233/21/8/085903>.
- Carlson HC. 2012. Sharpening our thinking about polar cap ionospheric patch morphology, research, and mitigation techniques. *Radio Sci* **47**(4): 1–16. <https://doi.org/10.1029/2011RS004946>.
- Carlson HC, Pedersen T, Basu S, Keskinen M, Moen J. 2007. Case for a new process, not mechanism, for cusp irregularity production. *J Geophys Res Space Phys* **112**(A11). <https://doi.org/10.1029/2007JA012384>.
- Crowley G, Schoendorf J, Roble RG, Marcos FA. 1996. Cellular structures in the high-latitude thermosphere. *J Geophys Res Space Phys* **101**(A1): 211–223. <https://doi.org/10.1029/95JA02584>.
- Di Mare F, Spicher A, Clausen LBN, Miloch WJ, Moen JI. 2021. Turbulence and intermittency in the Winter cusp ionosphere studied with the ICI sounding rockets. *J Geophys Res Space Phys* **126**(8): e2021JA029150. <https://doi.org/10.1029/2021JA029150>.
- Frisch U, Kolmogorov AN. 1995. *Turbulence: the legacy of AN Kolmogorov*. Cambridge University Press.
- Guthrie J, Marchand R, Marholm S. 2021. Inference of plasma parameters from fixed-bias multi-needle Langmuir probes (m-NLP). *Meas Sci Technol* **32**(9):095906. <https://doi.org/10.1088/1361-6501/abf804>.
- Hoang H, Røed K, Bekkeng T, Moen J, Spicher A, Clausen L, Miloch W, Trondsen E, Pedersen A. 2018. A study of data analysis techniques for the multi-needle Langmuir probe. *Meas Sci Technol* **29**(6): 065906.
- Hysell D, Kelley M, Swartz W, Pfaff R, Swenson C. 1994. Steepened structures in equatorial spread F: 1. *New observations*. *J Geophys Res Space Phys* **99**(A5): 8827–8840. <https://doi.org/10.1029/93JA02961>.
- Ivarsen MF, Jin Y, Spicher A, Clausen LB. 2019. Direct evidence for the dissipation of small-scale ionospheric plasma structures by a conductive E region. *J Geophys Res Space Phys* **124**(4): 2935–2942. <https://doi.org/10.1029/2019JA026500>.
- Ivarsen MF, St-Maurice J-P, Jin Y, Park J, Miloch W, Spicher A, Kwak Y-S, Clausen LB. 2021. Steepening plasma density spectra in the ionosphere: The crucial role played by a strong E-region. *J Geophys Res Space Phys* **126**(8): e2021JA029401. <https://doi.org/10.1029/2021JA029401>.
- Jacobsen K, Pedersen A, Moen J, Bekkeng T. 2010. A new Langmuir probe concept for rapid sampling of space plasma electron density. *Meas Sci Technol* **21**(8): 085902. <https://doi.org/10.1088/0957-0233/21/8/085902>.
- Jahn J-M, LaBelle J. 1998. Rocket measurements of high-altitude spread F irregularities at the magnetic dip equator. *J Geophys Res Space Phys* **103**(A10): 23427–23441. <https://doi.org/10.1029/97JA02636>.
- Jin Y, Moen JI, Miloch WJ. 2014. GPS scintillation effects associated with polar cap patches and substorm auroral activity: Direct comparison. *J Space Weather Space Clim* **4**: A23. <https://doi.org/10.1051/swsc/2014019>.

- Jin Y, Moen JI, Miloch WJ. 2015. On the collocation of the cusp aurora and the GPS phase scintillation: A statistical study. *J Geophys Res Space Phys* **120**(10): 9176–9191. <https://doi.org/10.1002/2015JA021449>.
- Kelley M, Pfaff R, Baker K, Ulwick J, Livingston R, Rino C, Tsunoda R. 1982a. Simultaneous rocket probe and radar measurements of equatorial spread F – Transitional and short wavelength results. *J Geophys Res Space Phys* **87**(A3): 1575–1588. <https://doi.org/10.1029/JA087iA03p01575>.
- Kelley MC, Vickrey JF, Carlson C, Torbert R. 1982b. On the origin and spatial extent of high-latitude F region irregularities. *J Geophys Res Space Phys* **87**(A6): 4469–4475. <https://doi.org/10.1029/JA087iA06p04469>.
- Keskinen MJ, Ossakow S. 1983. Theories of high-latitude ionospheric irregularities: A review. *Radio Sci* **18**(06): 1077–1091. <https://doi.org/10.1029/rs018i006p01077>.
- Kintner PM, Ledvina BM, De Paula E. 2007. GPS and ionospheric scintillations. *Space Weather* **5**(9). <https://doi.org/10.1029/2006SW000260>.
- Kintner PM, Seyler CE. 1985. The status of observations and theory of high latitude ionospheric and magnetospheric plasma turbulence. *Space Sci Rev* **41**(1): 91–129. <https://doi.org/10.1007/bf00241347>.
- LaBelle J, Kelley M, Seyler C. 1986. An analysis of the role of drift waves in equatorial spread F. *J Geophys Res Space Phys* **91**(A5): 5513–5525. <https://doi.org/10.1029/JA091iA05p05513>.
- Marholm S. 2020. *The unstructured particle-in-cell method with applications for objects in ionospheric plasmas*. Available at <http://urn.nb.no/URN:NBN:no-76155>.
- Marholm S, Marchand R. 2020. Finite-length effects on cylindrical Langmuir probes. *Phys Rev Res* **2**(2): 023016. <https://doi.org/10.1103/PhysRevResearch.2.023016>.
- Moen J, Oksavik K, Abe T, Lester M, Saito Y, Bekkeng T, Jacobsen K. 2012. First in-situ measurements of HF radar echoing targets. *Geophys Res Lett* **39**(7). <https://doi.org/10.1029/2012GL051407>.
- Moen J, Oksavik K, Alfonsi L, Daabakk Y, Romano V, Spogli L. 2013. Space weather challenges of the polar cap ionosphere. *J Space Weather Space Clim* **3**: A02. <https://doi.org/10.1051/swsc/2013025>.
- Moen J, Spicher A, Rowland D, Kletzing C, LaBelle J. 2018. *Grand Challenge Initiative – Cusp: Rockets to explore solar wind-driven dynamics of the top side polar atmosphere*. Available at [https://sios-svalbard.org/sites/sios-svalbard.org/files/common/SESS\\_2018\\_09\\_GCI\\_Cusp.pdf](https://sios-svalbard.org/sites/sios-svalbard.org/files/common/SESS_2018_09_GCI_Cusp.pdf).
- Moen J, Walker I, Kersley L, Milan S. 2002. On the generation of cusp HF backscatter irregularities. *J Geophys Res Space Phys* **107**(A4): SIA 3-1–3-5. <https://doi.org/10.1029/2001JA000111>.
- Moser C, LaBelle J, Roglans R, Bonnell J, Cairns I, Feltman C, Kletzing C, Bounds S, Sawyer R, Fuselier S. 2021. Modulated upper-hybrid waves coincident with lower-hybrid waves in the cusp. *J Geophys Res Space Phys* **126**(9): e2021JA029590. <https://doi.org/10.1029/2021JA029590>.
- Oksavik K, Moen J, Lester M, Bekkeng TA, Bekkeng JK. 2012. In situ measurements of plasma irregularity growth in the cusp ionosphere. *J Geophys Res Space Phys* **117**(A11): n/a–n/a. <https://doi.org/10.1029/2012ja017835>.
- Spicher A, LaBelle J, Bonnell JW, Roglans R, Moser C, et al. 2022. Interferometric study of ionospheric plasma irregularities in regions of phase scintillations and HF backscatter. *Geophys Res Lett* **49**(12): e2021GL097013. <https://doi.org/10.1029/2021GL097013>.
- Spicher A, Miloch W, Moen J. 2014. Direct evidence of double-slope power spectra in the high-latitude ionospheric plasma. *Geophys Res Lett* **41**(5): 1406–1412. <https://doi.org/10.1002/2014GL059214>.
- Takahashi T, Spicher A, Di Mare F, Rowland DE, Pfaff RF, Collier MR, Clausen LBN, Moen JI. 2022. Suppression of ionospheric irregularity due to auroral particle impact. *J Geophys Res Space Phys* **127**(1): e2020JA028725. <https://doi.org/10.1029/2020JA028725>.
- Tsunoda RT. 1988. High-latitude F region irregularities: A review and synthesis. *Rev Geophys* **26**(4): 719–760. <https://doi.org/10.1029/RG026i004p00719>.
- Villain J, Hanuise C, Beghin C. 1986. ARCAD3-SAFARI coordinated study of auroral and polar F-region ionospheric irregularities. *Ann Geophys* **4**: 61–68.
- Yeh KC, Liu C-H. 1982. Radio wave scintillations in the ionosphere. *Proc IEEE* **70**(4): 324–360. <https://doi.org/10.1109/PROC.1982.12313>.

## Appendix

### Normalization factors

Table A1 in Appendix shows the normalization factors of order  $10^{15}$  for the integrated power plots (Figs. 4g–4j). As the power was integrated with respect to different frequency intervals of different sizes (10 and 100 Hz), we decided to make the four plots more compatible. This was achieved by first dividing the integrated power by the length of the frequency interval (namely by a factor 10 for the frequencies between 10 Hz and 100 Hz (Figs. 4g and 4h) and a factor 100 for the frequencies between 100 Hz and 1000 Hz (Figs. 4i and 4j). This provided a result in power/Hz. As a power spectrum is naturally cascading to lower values for higher frequencies, we were interested in a change of integrated power instead of absolute power. Due to the cascading and integrated power for 10 Hz would naturally always be higher than for 20 Hz and so forth. In order to look at the relative fluctuations in integrated power we divided each graph (corresponding to the integrated power/Hz for each frequency interval) by the median of a “quiet area” of the same graph.

The 50 Hz graph of the high flyer (green graph in Figs. 4g) shall be taken as an example. In order to compare the intervals of 10 Hz length to the intervals of 100 Hz length, we first divide this graph by 10. The integral of a power spectrum between 50 Hz and 60 Hz would naturally be much smaller than the integral between 20 Hz and 30 Hz but much bigger than an interval between 70 Hz and 80 Hz. In order to compare these intervals in a better way with each other, we divide every graph by the median of itself in a quiet interval (an interval without many fluctuations in integrated power). This way, all graphs should be normalized to a similar “base line” (this means that the quiet areas of the integrated power all have roughly the same value. If no normalization was done, all graphs would have different values for the quiet areas). All graphs were normalized with a median taken from the same time interval, which corresponds to a minute of data 300–360 s into the flight. This is the interval between 08:31:00 and 08:32:00 UT for the high flyer and between 08:33:00 and 08:34:00 UT for the low flyer. Each graph was then divided by its corresponding normalization factor, all factors can be found in Table A1.

**Table A1.** Normalization factors for integrated power as seen in Figure 4g, 4h, 4i, and 4j. The normalization factors consist of the median of each frequency interval and the interval length, the factors are of order  $10^{15}$ .

	High flyer	Low flyer		High flyer	Low flyer
10–19 Hz	1.07	1.07	100–199 Hz	7.42	7.50
20–29 Hz	0.49	0.38	200–299 Hz	6.50	6.43
30–39 Hz	0.36	0.24	300–399 Hz	6.48	6.29
40–49 Hz	0.22	0.25	400–499 Hz	6.50	6.18
50–59 Hz	0.22	0.14	500–599 Hz	6.50	6.41
60–69 Hz	0.17	0.14	600–699 Hz	6.24	6.44
70–79 Hz	0.13	0.11	700–799 Hz	6.26	6.53
80–89 Hz	0.11	0.11	800–899 Hz	6.00	6.13
90–99 Hz	0.11	0.09	900–999 Hz	5.69	5.71

**Cite this article as:** Buschmann LM, Bonnell JW, Bounds S, Clausen LBN, Kletzing C, et al. 2023. The role of particle precipitation on plasma structuring at different altitudes by in-situ measurements. *J. Space Weather Space Clim.* **13**, 13. <https://doi.org/10.1051/swsc/2023012>.